New Journal of Physics
The open-access journal for physics

Circuital model for the spherical geodesic waveguide perfect drain

Juan C González[1], **Dejan Grabovičkić, Pablo Benítez and Juan C Miñano**

Universidad Politécnica de Madrid, Cedint, Campus de Montegancedo, 28223 Madrid, Spain
E-mail: jcgonzalez@cedint.upm.es

New Journal of Physics **14** (2012) 083033 (19pp)
Received 17 May 2012
Published 24 August 2012
Online at http://www.njp.org/
doi:10.1088/1367-2630/14/8/083033

Abstract. The perfect drain for the Maxwell fish eye (MFE) is a non-magnetic dissipative region placed in the focal point to absorb all the incident radiation without reflection or scattering. The perfect drain was recently designed as a material with complex permittivity that depends on frequency. However, this material is only a theoretical material, so it cannot be used in practical devices. The perfect drain has been claimed as necessary for achieving super-resolution (Leonhardt 2009 *New J. Phys.* **11** 093040), which has increased the interest in practical perfect drains suitable for manufacturing. Here, we present a practical perfect drain that is designed using a simple circuit (made of a resistance and a capacitor) connected to the coaxial line. Moreover, we analyze the super-resolution properties of a device equivalent to the MFE, known as a spherical geodesic waveguide, loaded with this perfect drain. The super-resolution analysis for this device is carried out using COMSOL Multiphysics. The results of simulations predict a super-resolution of up to $\lambda/3000$.

[1] Author to whom any correspondence should be addressed.

Contents

1. Introduction

The term 'super-resolution' refers to the capacity of an optical system to produce images with details below the classic Abbe diffraction limit. Over the last decade, super-resolution has been demonstrated experimentally with devices made of left-handed materials [1, 2] (i.e. materials with negative dielectric and magnetic constants) [3, 4]. Super-resolution has also been achieved using devices made of microstructured magnetic materials (see, for example, [5] where RF flux has been guided for a remote object to the receiver coil in a magnetic resonance imaging machine).

An alternative device for perfect imaging has recently been proposed [7, 8]: the Maxwell fish eye (MFE) lens. Unlike previous perfect imaging devices, the MFE uses materials with a positive, isotropic refractive index distribution. This device is very well known within the framework of geometrical optics because it is an absolute instrument [6], so every object point has a stigmatic image point.

Leonhardt [7] analyzed the Helmholtz wave fields in the MFE lens in two dimensions (2D). These Helmholtz wave fields describe TE-polarized modes in a cylindrical MFE, i.e. modes in which the electric field vector points orthogonally to the cross-section of the cylinder. Leonhardt found a family of Helmholtz wave fields which have monopole asymptotic behavior at an object point as well as at its stigmatic image point. Each one of these solutions describes a wave propagating from the object point to the image point. It coincides asymptotically with an outward (monopole) Helmholtz wave at the object point, as generated by a point source, and with an inward (monopole) wave at the image point, as it was sunk by an 'infinitely well localized drain' (which we call a 'perfect point drain'). This perfect point drain absorbs the incident wave, with no reflection or scattering. This result has also been confirmed via a different approach [9].

The physical significance of a passive perfect point drain has been controversial [10–19]. In [7] and [6] the perfect point drain was not physically described, but only considered as a

mathematical entity (a point drain is represented by Dirac-delta as the point source). However, a rigorous example of a passive perfect point drain for the MFE has recently been found, clarifying the controversy [20]. It consists of a dissipative region whose diameter tends toward zero and whose complex permittivity ε takes a specific value depending on the operation frequency.

One experiment has recently been carried out to support the super-resolution capability in the MFE. Super-resolution with positive refraction has been demonstrated for the very first time at a microwave frequency ($\lambda = 3$ cm) [21, 22]. The experimental results showed that two sources at a distance of $\lambda/5$ from each other (where λ denotes the local wavelength $\lambda = \lambda_0/n$) could be resolved with an array made up of ten drains spaced $\lambda/20$. The distance between the sources ($\lambda/5$) is smaller than the classic diffraction limit ($\sim\lambda/2.5$).

Although the perfect drain has not been used in these experiments, i.e. there was a reflected wave from the drain to the source, the MFE has shown super-resolution at microwave frequencies. This means that the perfect drain is not necessary for achieving super-resolution (see also [23]).

Recently, a device equivalent to the MFE, the spherical geodesic waveguide (SGW) made for microwave frequencies, has been presented [23, 24]. The SGW is a spherical waveguide filled with a non-magnetic material and isotropic refractive index distribution proportional to $1/r(\varepsilon = (r_0/r)^2$ and $\mu = 1)$, r being the distance to the center of the spheres. Transformation optics theory [25] proves that the TE-polarized electric modes of the cylindrical MFE are transformed into radial-polarized modes in the SGW, so both have the same imaging properties. When the waveguide thickness is small enough, the variation in the refractive index within the two spherical shells can be ignored, resulting in a constant refractive index within the waveguide. In [23], the SGW has been analyzed using two coaxial ports (source and drain) loaded with the characteristic impedances. The results have shown a super-resolution up to $\lambda/500$ for a discrete number of frequencies, called notch frequencies, which are close to the well-known Schumann resonance frequencies of spherical systems. For other frequencies the system did not present a resolution below the diffraction limit. In this analysis, the perfect drain has not been used; thus, in addition to the incident wave, there is also a reflected wave in the SGW. However, super-resolution properties have been shown.

In this paper, we present an improvement in super-resolution achieved using the SGW with the perfect drain. The perfect drain is implemented using a circuit (made of a resistor and a capacitor) connected to the drain coaxial port. The difference between the presented drain and the perfect drain proposed in [20] lies in the practical implementation. Whereas in [20] the perfect drain is made of a material with complex permittivity ε, here it is only a coaxial port loaded with a resistor and a capacitor of conventional values (e.g. $R = 2.57\,\Omega$ and $C = 55.05$ pF for $f = 0.25$ GHz). Using the circuital model for the perfect drain, the COMSOL simulations have shown the following two results that improve the super-resolution properties of the device analyzed in [23].

1. A super-resolution of up to $\lambda/3000$ for the same discrete frequencies as in [23], which is much higher than the $\lambda/500$ obtained without the perfect drain.
2. A bandwidth of super-resolution that is 20 times higher than in the case reported in [23].

In section 2, the microwave circuit, the concept of perfect drain and its circuital model are described. In section 3, we present a simulation of the SGW loaded with the perfect drain. The discussion and conclusions are presented in section 4. The complete modal analysis of the SGW, including the rigorous procedure used to find the perfect drain and the analysis of the transmitted

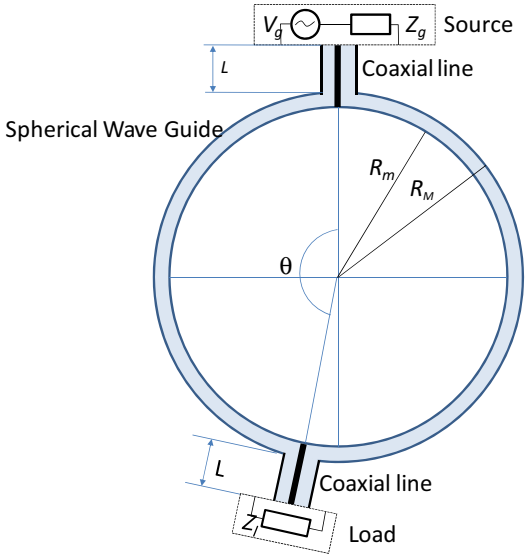

Figure 1. Microwave circuit analyzed in this paper. It comprises the following: the source (V_g and Z_g) connected to a coaxial transmission line of length L, the load (Z_l) connected to the other identical transmission line and the spherical waveguide. R_M and R_m are the radii of the external and internal metallic spheres.

and evanescent modes, is described in appendix A. Finally, in appendix B the voltage and current waves are defined in the same manner as in classical transmission lines theory.

2. Microwave circuit and parameters of the simulation

The SGW is bounded by two metallic spherical shells. The medium between the shells is air. Two coaxial ports have been used to simulate the source and the drain in the SGW. Consider that the microwave circuit consists of the voltage generator V_g with the impedance Z_g (on the source port side), coaxial ports, the SGW and the load with the impedance Z_l (on the drain port side), as shown in figure 1.

Let us define the merit function M as

$$M = \frac{P_{\text{load}}}{P_{\text{max}}}, \tag{1}$$

where P_{load} is the power delivered to the load Z_l and P_{max} is the maximum power that can be delivered by the generator [26]. This circuit coincides with the one analyzed in [23] with the condition $Z_l = Z_g = Z_0$, where Z_0 is the characteristic impedance of the coaxial lines. In this case, it can be easily proven that $M = |S_{21}|^2$ where S_{21} is the scattering parameter of the circuit [26].

In this paper, we are going to analyze the circuit in figure 1 with Z_l and Z_g different from Z_0 (and then M is different from $|S_{21}|^2$). The reason for this is that we are going to use a specific value of impedance Z_{pd} that simulates the perfect drain introduced by Leonhardt in [7], which is described next. In order to make a comparison with the results in [23], we have used the impedances $Z_l = Z_g = Z_{\text{pd}}$ (instead of $Z_l = Z_g = Z_0$ of [23]).

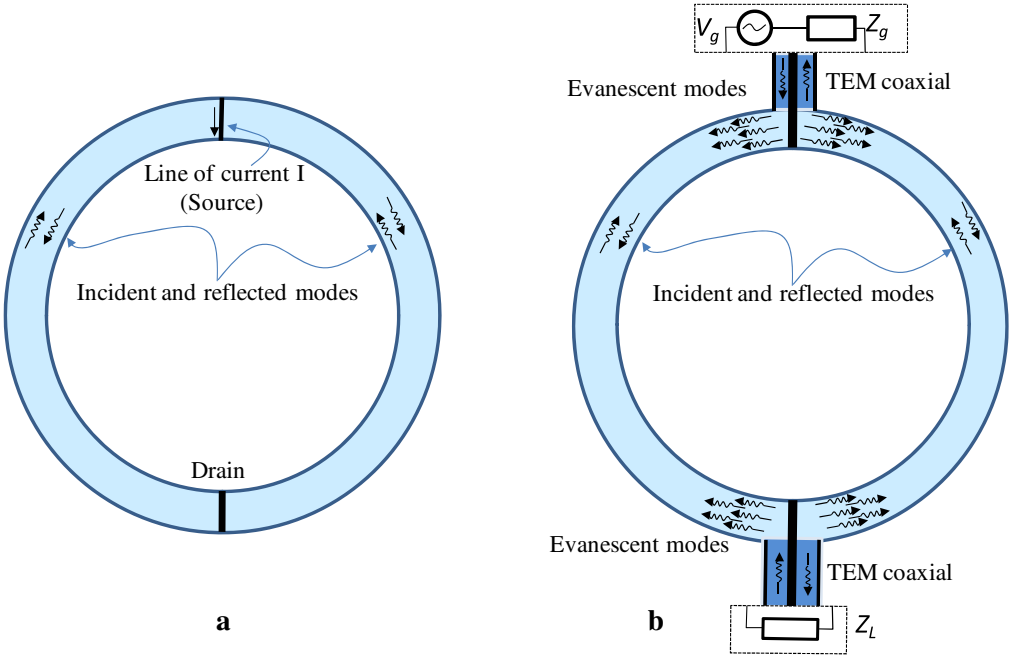

Figure 2. Ideal structure (a) and structure formed by the SGW, coaxial port and impedances (b). The incident and reflected modes are the same in both structures. In (a), the perfect drain is the material of complex permittivity ε, and in (b), the impedance Z_1 does not produce any reflected wave.

2.1. Incident and reflected modes in the spherical geodesic waveguide (SGW)

In order to calculate the perfect drain impedance Z_{pd}, let us consider now the drain port centered at the source's image point (i.e. $\theta = \pi$ in figure 1), a situation in which the electromagnetic fields will have rotational symmetry with respect to the source–drain line axis.

Figure 2(a) shows an idealized physical model of the SGW in which we can consider that the source is a line current in between the two metallic spheres at $\theta = 0$, and the drain is made up of a non-magnetic dissipative material placed in the region $\theta > \pi - \theta_1$, where $\theta_1 \to 0$. In figure 2(a), incident and reflected modes are shown, which correspond to the general case for an arbitrary dissipative material. For a specific complex value ε, the incident mode is totally absorbed (so there is no reflected mode), which is the perfect drain discussed in [23]. The incident and reflected modes are given by [23]

$$\begin{aligned}
&\mathbf{E}(r,\theta) = k_0^2\left[A_0 F_{\nu_0}(\cos(\theta)) + B_0 R_{\nu_0}(\cos(\theta))\right]\mathbf{r},\\
&\mathbf{H}(r,\theta) = -\mathrm{i}\omega\varepsilon_0\left[A_0 F'_{\nu_0}(\cos(\theta)) + B_0 R'_{\nu 0}(\cos(\theta))\right]\frac{1}{r}\phi,\\
&F_{\nu_0}(x) = P_{\nu_0}(x) + \mathrm{i}\frac{2}{\pi}Q_{\nu_0}(x), \qquad R_{\nu_0}(x) = P_{\nu_0}(x) - \mathrm{i}\frac{2}{\pi}Q_{\nu_0}(x),\\
&\nu_0 = -0.5 + 0.5\sqrt{1 + 4(R_{\mathrm{M}}k_0)^2}, \qquad k_0 = \frac{2\pi}{\lambda},
\end{aligned} \tag{2}$$

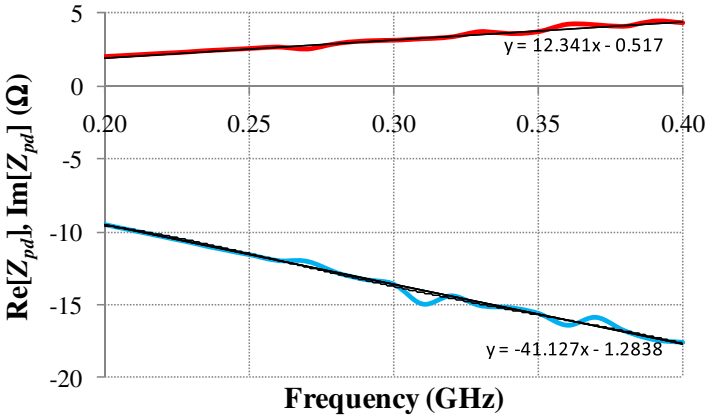

Figure 3. Real (in red) and imaginary (in blue) parts of the perfect drain impedance for different frequencies.

where A_0 and B_0 are complex constants, R_M is the outer sphere radius, $P_{\nu 0}$ and $Q_{\nu 0}$ are the Legendre function of the first and second kind and $F_{\nu 0}$ and $R_{\nu 0}$ are the running-wave Legendre functions [27]. The power transmitted through a surface $\theta =$ constant is

$$P = \mathrm{Re}\left[\iint_{\substack{R_m<r<R_M \\ 0<\varphi<2\pi}} \frac{1}{2}(\mathbf{E}\times\mathbf{H}^*) r \sin(\theta) \mathrm{d}r\, \mathrm{d}\varphi \right] = 2k_0^2 \omega\varepsilon (R_M - R_m)(|A_0|^2 - |B_0|^2), \tag{3}$$

which shows clearly that $F_{\nu 0}$ and $R_{\nu 0}$ are the incident and reflected modes.

Figure 2(b) shows the physical model described in figure 1 for the case $\theta = \pi$, which is the one to be analyzed in section 3. According to the modal analysis shown in appendix A, only the same two modes $F_{\nu 0}$ and $R_{\nu 0}$ are transmitted inside the SGW, although there are other evanescent modes in the vicinity of the source and drain ports.

2.2. Perfect drain impedance Z_{pd}

The perfect drain must produce $B_0 = 0$ in (3), that is, no reflected mode inside the SGW. The procedure used to find the load $Z_l = Z_{pd}$ that simulates the perfect drain is described in detail in appendix A. Figure 3 shows both the real and imaginary parts of Z_{pd} calculated for the physical characteristics of the device and the band of frequencies simulated here (0.2–0.4 GHz, $R_M = 1005$ mm, $R_m = 1000$ mm, $a = 5$ mm, $b = 10$ mm and $L = 20$ mm; see figures 1 and A.1). The results show some oscillation resulting from numerical errors in the calculation, but linear approximations can be used. That impedance can be identified with an R–C circuit, $Z_{pd} = R - \mathrm{i}/\omega C$, in which R and C vary with ω.

3. Super-resolution analysis of the spherical geodesic waveguide matched with the perfect drain

The SGW with the perfect drain is designed and analyzed in COMSOL. In order to show super-resolution properties of the SGW, we have carried out several simulations for different

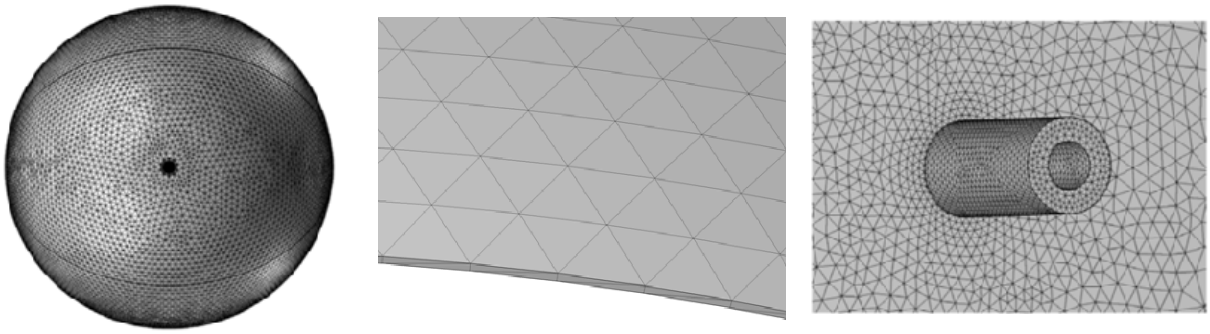

(a) (b) (c)

Figure 4. Mesh structure. (a) SGW with a coaxial port, (b) close-up of a piece of the spherical shells, (c) close-up of one coaxial port from outside the sphere.

displacements of the drain port, and for different frequency values. Special care has been taken to define the mesh of the system. In order to mesh the guide properly, the geometry has been divided into a few domains. Each domain is meshed separately according to its geometric and physical properties. Since the guide thickness is very low $(R_M - R_m)/R_m = 1$, the SGW is meshed using a swept mesh (2D triangular mesh from the outer surface is swept to the inner surface, see figure 4(b)). On the other hand, the coaxial line is meshed with higher density using 3D tetrahedra. The mesh density is increased since the change in the electric field is significant in the vicinity of the coaxial port.

The dimensions of the structure analyzed here are (figures 1 and A.1)

- $R_M = 1005$ mm,
- $R_m = 1000$ mm,
- $a = 5$ mm ($\theta_a = 0.285^\circ$),
- $b = 10$ mm ($\theta_b = 0.57^\circ$),
- $L = 20$ mm.

3.1. M as a function of frequencies for different positions of the drain

We have computed M using COMSOL for a frequency range between 0.2 and 0.4 GHz for different positions of the drain port. The source port is fixed at $\theta = 0$, whereas the drain port is shifted λ/N (for $\lambda = 1$ m corresponding to 0.3 GHz and $N > 100$) from the source's image point $\theta = \pi$ (see figure 1). When the drain port is placed in the image point, all the power is delivered perfectly. This can be achieved for all the frequencies using the corresponding perfect drain impedance. However, when the drain is moved from the image point, some of the power gets reflected, so the power delivered to the drain decreases. This power drop is extremely abrupt for some frequencies very close to the Schumann frequencies, called notch frequencies (see also [23]). Figure 5 shows M for different drain port positions in a very narrow band in the neighborhood of the notch frequency close to $\nu_0 = 5$. The curves correspond to different shifts in the drain port. The shifts are, in all cases, much smaller than wavelength (from $\lambda/100$ to $\lambda/3000$ with $\lambda = 1.150\,840\,47$ m that corresponds to $f = 0.260\,687\,4$ GHz, see figure 5).

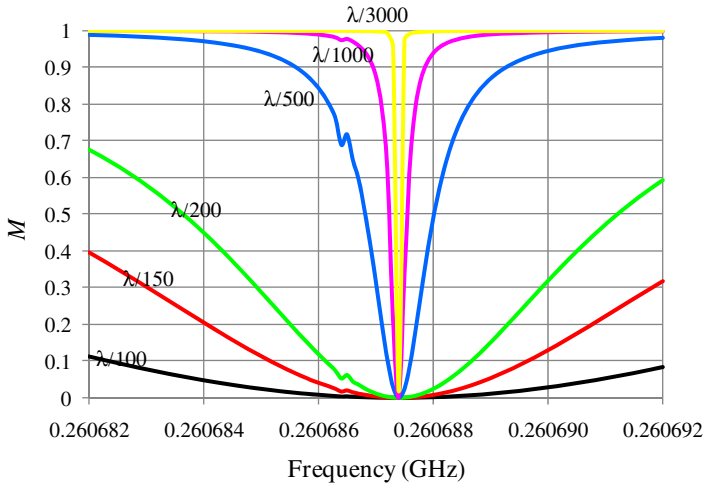

Figure 5. Detail of M as a function of frequency in a narrow band around a notch frequency for different drain port positions. The notch frequency is $f = 0.260\,687\,4$ GHz ($\nu = 4.996$). The nearest Schumann frequency is $f = 0.260\,866\,09$ GHz ($\nu = 5$), which is outside the range of this figure.

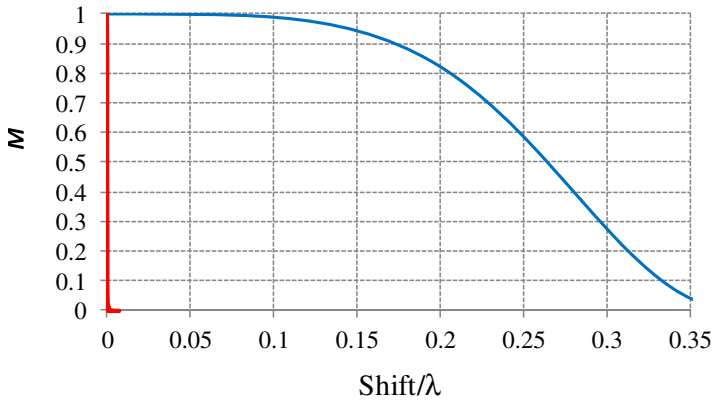

Figure 6. M as function of the drain port shift for a frequency near a notch one (red curve) and for a frequency far from the notch one (blue curve).

These results are quite surprising, since close to a specific frequency the power transmitted to the drain port suddenly reduces to a value near zero.

3.2. M as a function of the drain port shift for different frequencies

Since M is proportional to the transmitted power, the graph representing M versus the drain port shift (figure 6) is equivalent to the point spread function (PSF) commonly used in optics. This equivalence may seem surprising since the PSF is defined as the square of the electric field amplitude calculated in the absence of absorbers in the image space, and M is defined in terms of the power transmitted to an absorber. However, the equivalence comes from the fact that, in optics, the detection at the image is assumed to be made with a sensor that does not perturb the

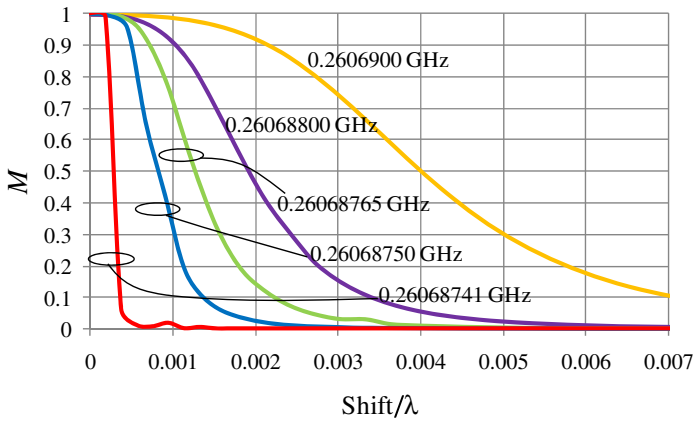

Figure 7. M as a function of the drain port shift for different frequencies corresponding to a super-resolution range between $\lambda/3000$ and $\lambda/140$.

free-space fields; or that even if it does perturb the fields, it is assumed that the sensor signal is still proportional to the field amplitude (or its square, which is the PSF). Figure 6 shows M versus the drain port shifts for two frequencies. The blue curve corresponds to $f = 0.2847$ GHz ($\nu_0 = 5.5$), i.e. far from a notch frequency.

Let us define 'resolution' as the arc length (in wavelength units) that a drain port needs to be shifted, so M drops to 10% (not far from the Rayleigh criteria in optics, which refers to the first null). With this definition, the diffraction-limited resolution given by the blue curve is $\lambda/3$. The red curve corresponds to notch frequency $f = 0.260\,687\,41$ GHz ($\nu_0 = 4.996$), which clearly shows a much better resolution ($\lambda/3000$).

Figure 7 is a blow-up of figure 6 in the upper neighborhood of a notch frequency. The graph for frequencies slightly below the notch frequency is similar. Note that figure 7 shows the same information as figure 5 but plotting M versus the drain port shift (expressed in units of λ) and using the frequency as a parameter. Increasing resolutions are achieved from the orange to the red curves: $\lambda/140$ for the orange to $\lambda/3000$ for the red. The latter, whose frequency $f = 0.260\,687\,41$ GHz corresponds to $\nu = 4.996\,36$, is the highest resolution that we have obtained. Computations for frequencies near the notch frequency show essentially null M values for shifts $>\lambda/3000$ (as in the red line in the picture). M values for shifts below $\lambda/3000$ (except null shift or shifts very close to zero) and frequencies near a notch frequency are inconsistent (the solver did not converge to a single solution due to numerical errors). It seems that Leonhardt's assertion of infinite resolution (i.e. perfect imaging) may occur for the discrete notch frequencies in the SGW, although the aforementioned inconsistencies have prevented us from numerically predicting resolutions beyond $\lambda/3000$.

The $\lambda/3000$ resolution is achieved only for a narrow bandwidth (≈ 10 Hz, which is much smaller than the notch frequency $\approx$0.3 GHz). If larger bandwidths are needed, lower resolutions (but still sub-wavelength) may be achieved. Figure 8 shows a plot of the bandwidth versus N, meaning that the resolution is better than λ/N. The bandwidth has been calculated as $f_{\max} - f_{\min}$ with $f_{\max}$ and $f_{\min}$ fulfilling $M(f_{\max}) = M(f_{\min}) = 0.1$, using the information of the curves in figure 5 and similar curves. The linear dependence shown in figure 8 (slope -2) reveals that the product $N^2 \times$ bandwidth is constant within the range analyzed here.

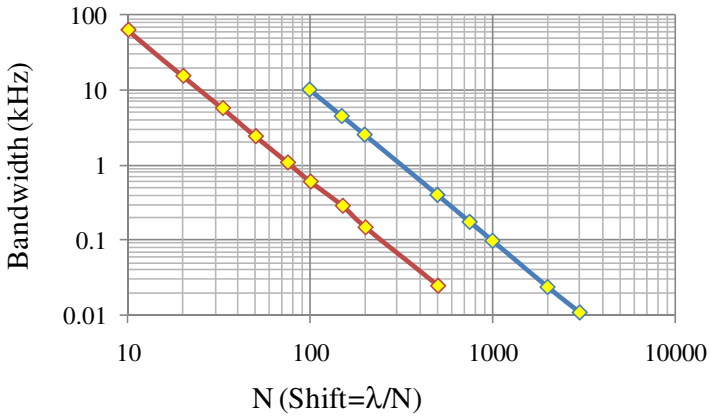

Figure 8. Bandwidth as a function of resolution. The abscissa axis shows N, meaning that the resolution is better than λ/N. The blue curve represents the results obtained using the perfect drain designed here, while the red curve represents the results obtained in the SGW loaded with the characteristic impedance which is the case analyzed in [23].

4. Discussion

Leonhardt [7, 8] has suggested that the MFE should produce perfect imaging for any frequency using perfect drains. However, the experiments in [21, 22] and simulations from [23] have shown super-resolution properties of the MFE, although the perfect drain has not been used. In these references, the coaxial ports were loaded with their characteristic impedances, so the absorption of the incident wave was not perfect. Leonhardt assumed that the ability of the MFE to propagate the wave, generated by a point source, toward to a perfect point drain was enough to guarantee perfect imaging. This does not seem to be sufficient, since it does not provide information on how much power the drain will absorb when it is displaced outside the image point. The simulations presented here show that super-resolution only takes place for a particular set of frequencies known as notch frequencies, the same as in [23]. The presented results have shown a maximum super-resolution of $\lambda/3000$, which is much higher than that in the case when there were no perfect drains ($\lambda/500$; see [23]). The frequency bandwidth has also increased 20 times, e.g. for $\lambda/500$ the bandwidth is about 400 Hz (figure 8), while in [23] it was only 20 Hz.

Acknowledgments

We thank the European Commission (SMETHODS: FP7-ICT-2009-7, grant agreement no. 288526; NGCPV: FP7-ENERGY.2011.1.1, grant agreement no. 283798), the Spanish Ministries (ENGINEERING METAMATERIALS: CSD2008-00066; DEFFIO: TEC2008-03773; ECOLUX: TSI-020100–2010-1131; SEM: TSI-020302–2010-65; SUPERRESOLUCION: TEC2011-24019; SIGMAMODULOS: IPT-2011–1441-920000; PMEL: IPT-2011-1212-920000) and the UPM (Q090935C59) for the support given to the research activities of the UPM-Optics Engineering Group, thereby making the present work possible.

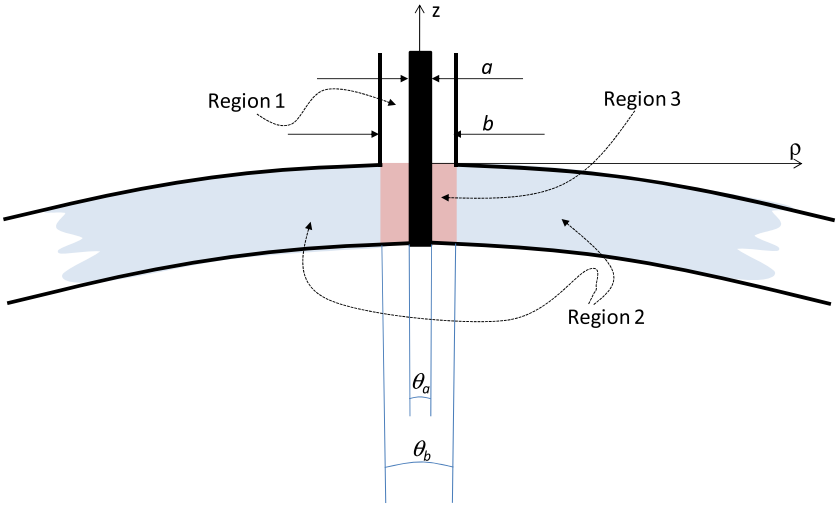

Figure A.1. Three regions of the junction used for the analysis. The coaxial is indicated by the white region, the SGW by the blue region and the common region by the red region. θ_a and θ_b are the angles in spherical coordinates covered by the inner and outer conductors of the coaxial.

Appendix A. Modal analysis of the structure and numerical procedure for finding the perfect drain

The perfect drain Z_{pd} absorbs all the incident radiation without reflection inside the SWG when the source and the drain are placed at opposite poles ($\theta = \pi$). In this section, we present a rigorous procedure to find this impedance for a wide band of frequencies.

A.1. Symmetry of the structure

The structure does not depend on the cylindrical (coaxial) and spherical (SWG) coordinate ϕ; thus:

- The only modes of the coaxial guide without ϕ dependence are the TEM modes, so in the interface between the coaxial and the sphere there are only the incident and reflected TEM modes [26].
- Inside the SGW, electric and magnetic fields are necessary of the form

$$\begin{aligned} \mathbf{E}(r,\theta) &= E_r(r,\theta)\mathbf{r} + E_\theta(r,\theta)\theta, \\ \mathbf{H}(r,\theta) &= H_\phi(r,\theta)\phi. \end{aligned} \tag{A.1}$$

A complete analysis of the modes is carried out using the same procedure as that explained by Wu and Ruan [28] on a radial-line/coaxial-line junction. Figure A.1 shows the complete region of the junction separated into three smaller regions: the coaxial (region 1), the SGW (region 2) and the common region (region 3). The electronic field is calculated in each of these three regions using the procedure described below.

A.2. The field in the coaxial line (region 1)

Because of the symmetry of the structure, the field of the coaxial port is completely described by the TEM modes of the line [26]:

$$\mathbf{E} = \left(\frac{V_e^+}{\rho Ln(b/a)}e^{-jk_0 z} + \frac{V_e^-}{\rho Ln(b/a)}e^{jk_0 z}\right)\rho,$$
$$\mathbf{H} = \frac{1}{\sqrt{\mu/\varepsilon}}\left(\frac{V_e^+}{\rho Ln(b/a)}e^{-jk_0 z} - \frac{V_e^-}{\rho Ln(b/a)}e^{jk_o z}\right)\phi, \tag{A.2}$$

where a and b are the diameters of the internal and the external coaxial (figure A.1), ρ and z the cylindrical coordinates, k_0 the propagation constant and V_e^+ and V_e^- constants. With the condition $b = R_M$, on the surface $z = 0$ (figures 1 and A.1), the fields can be approximated to

$$\mathbf{E} = \left(\frac{V_e^+}{R_M \sin(\theta) Ln(b/a)} + \frac{V_e^-}{R_M \sin(\theta) Ln(b/a)}\right)\theta,$$
$$\mathbf{H} = \frac{1}{\sqrt{\mu/\varepsilon}}\left(\frac{V_e^+}{R_M \sin(\theta) Ln(b/a)} - \frac{V_e^-}{R_M \sin(\theta) Ln(b/a)}\right)\varphi, \tag{A.3}$$

where θ and φ are the spherical coordinates.

A.3. The field in the spherical geodesic waveguide (region 2)

With the condition $R_M - R_m = R_M$, one complete set of solutions inside the SWG fulfilling the boundary condition of metallic surfaces is [29]

$$E_r(r,\theta) = \sum_n \left[A_n F_{\nu_n}(\cos(\theta)) + B_n R_{\nu_n}(\cos(\theta))\right]\left(\left(\frac{n\pi}{R_M - R_m}\right)^2 + k_0^2\right)\left(-\cos\left(\frac{(r - R_m)n\pi}{R_M - R_m}\right)\right),$$
$$E_\theta(r,\theta) = \sum_n \frac{1}{r}\left[A_n F'_{\nu_n}(\cos(\theta)) + B_n R'_{\nu_n}(\cos(\theta))\right]\frac{-n\pi}{R_M - R_m}\sin\left(\frac{(r - R_m)n\pi}{R_M - R_m}\right),$$
$$H_\varphi(r,\theta) = -i\omega\varepsilon_0 \sum_n \left[A_n F'_{\nu_n}(\cos(\theta)) + B_n R'_{\nu_n}(\cos(\theta))\right]\frac{1}{r}\cos\left(\frac{(r - R_m)n\pi}{R_M - R_m}\right), \tag{A.4}$$
$$\nu_n \approx -0.5 + 0.5\sqrt{1 + 4\left((R_M k_0)^2 - \left(\frac{R_M n\pi}{R_M - R_m}\right)^2\right)},$$

where A_n and B_n are constants and F_{ν_n} and R_{ν_n} are called the forward and reverse functions defined as

$$F_{\nu_n}(x) = P_{\nu_n}(x) + i\frac{2}{\pi}Q_{\nu_n}(x),$$
$$R_{\nu_n}(x) = P_{\nu_n}(x) - i\frac{2}{\pi}Q_{\nu_n}(x), \tag{A.5}$$

and P_{ν_n} and Q_{ν_n} are the Legendre functions of the first and second kind.

A.4. The field in the common region of coaxial and spherical geodesic waveguide (region 3)

The solution in this region has the same form as the solution expressed in (A.4), but now having an additional term, one particular solution, necessary for fulfilling the boundary conditions on the common surfaces.

$$E_r(r,\theta)=\sum_n\left[D_nF_{\nu_n}(\cos(\theta)+E_nR_{\nu_n}(\cos(\theta))\right]\left(\left(\frac{n\pi}{R_\mathrm{M}-R_\mathrm{m}}\right)^2+k_0^2\right)\left(-\cos\left(\frac{(r-R_\mathrm{m})n\pi}{R_\mathrm{M}-R_\mathrm{m}}\right)\right),$$

$$E_\theta(r,\theta)=E_p(r,\theta)+\sum_n\frac{1}{r}\left[D_nF'_{\nu_n}(\cos(\theta)+E_nR'_{\nu_n}(\cos(\theta))\right]\frac{-n\pi}{R_\mathrm{M}-R_\mathrm{m}}\sin\left(\frac{(r-R_\mathrm{m})n\pi}{R_\mathrm{M}-R_\mathrm{m}}\right),$$

$$H_\varphi(r,\theta)=H_p(r,\theta)-\mathrm{i}\omega\varepsilon_0\sum_n\left[D_nF'_{\nu_n}(\cos(\theta)+E_nR'_{\nu_n}(\cos(\theta))\right]\frac{1}{r}\cos\left(\frac{(r-R_\mathrm{m})n\pi}{R_\mathrm{M}-R_\mathrm{m}}\right),\tag{A.6}$$

where the particular solutions for E_p and H_p have to fulfil the Maxwell equations and the boundary conditions at $r=R_\mathrm{M}$ and $r=R_\mathrm{m}$.

$$\mathbf{E_p}=E_p(r,\theta)\theta,\quad \nabla\times\mathbf{E_p}=\frac{1}{r}\frac{\partial}{\partial r}(rE_p(r,\theta))\varphi=-\mathrm{i}\omega\mu\mathbf{H_p}(r,\theta),$$

$$\nabla\times\mathbf{H_p}=\frac{-1}{\mathrm{i}\omega\mu}\frac{1}{r^2\sin(\theta)}\frac{\partial}{\partial\theta}\left(\sin(\theta)\frac{\partial}{\partial r}(rE_p(r,\theta))\right)\mathbf{r}+\frac{1}{\mathrm{i}\omega\mu}\frac{1}{r}\frac{\partial}{\partial r}\left(\frac{\partial}{\partial r}(rE_p(r,\theta))\right)\theta$$
$$=\mathrm{i}\omega\varepsilon E_p(r,\theta)\theta.\tag{A.7}$$

From the second equation in (A.7), it is necessary that

$$E_p(r,\theta)=f(r)\frac{1}{\sin(\theta)},$$
$$\frac{\mathrm{d}^2}{\mathrm{d}r^2}(\mathrm{rf}(r))=-k_0^2\,\mathrm{rf}(r),\tag{A.8}$$
$$k_0^2=\omega^2\mu\varepsilon.$$

Solving the differential equation from (A.8), the particular solutions for the fields E_p and H_p are obtained:

$$E_p(r,\theta)=\frac{a_1\frac{\mathrm{e}^{\mathrm{i}k_0r}}{r}+a_2\frac{\mathrm{e}^{-\mathrm{i}k_0r}}{r}}{\sin(\theta)},\quad H_\mathrm{p}(r,\theta)=\frac{-\mathrm{i}k_0}{\mathrm{i}\omega\mu}\frac{a_1\frac{\mathrm{e}^{\mathrm{i}k_0r}}{r}-a_2\frac{\mathrm{e}^{\mathrm{i}k_0r}}{r}}{\sin(\theta)},\tag{A.9}$$

where a_1 and a_2 are two integration constants. These constants are obtained by using the boundary conditions for E_p at $r=R_\mathrm{M}$ (A.3) and $r=R_\mathrm{m}$ ($E_p=0$ for the metallic surface):

$$a_1=(V_e^+ + V_e^-)\frac{1}{\mathrm{Ln}(b/a)}\left(\frac{1}{\mathrm{e}^{\mathrm{i}k_0R_\mathrm{M}}-\mathrm{e}^{\mathrm{i}k_0(2R_\mathrm{m}-R_\mathrm{M})}}\right),$$
$$a_2=(V_e^+ + V_e^-)\frac{1}{\mathrm{Ln}(b/a)}\left(\frac{-\mathrm{e}^{\mathrm{i}k_02R_\mathrm{m}}}{\mathrm{e}^{\mathrm{i}k_0R_\mathrm{M}}-\mathrm{e}^{\mathrm{i}k_0(2R_\mathrm{m}-R_\mathrm{M})}}\right).\tag{A.10}$$

The fields defined in (A.9) and (A.10) can be expanded as a series:

$$E_p(r,\theta) = \frac{V_e^+ + V_e^-}{r\ \sin(\theta)} \sum_n d_n \frac{-n\pi}{R_\mathrm{M} - R_\mathrm{m}}\ \sin\left[\frac{(r-R_\mathrm{m})n\pi}{R_\mathrm{M}-R_\mathrm{m}}\right],$$
$$H_p(r,\theta) = \frac{V_e^+ + V_e^-}{r\sin(\theta)} \sum_n e_n\ \cos\left[\frac{(r-R_\mathrm{m})n\pi}{R_\mathrm{M}-R_\mathrm{m}}\right], \tag{A.11}$$

where d_n and e_n are the expansion constants satisfying $j\omega\varepsilon d_n = -e_n$. The complete field in this region is then

$$E_r(r,\theta) = \sum_n \left[D_n F_{\nu_n}(\cos(\theta) + E_n R_{\nu_n}(\cos(\theta))\right]\left(\left(\frac{n\pi}{R_\mathrm{M}-R_\mathrm{m}}\right)^2 + k_0^2\right)\left(-\cos\left(\frac{(r-R_\mathrm{m})n\pi}{R_\mathrm{M}-R_\mathrm{m}}\right)\right),$$
$$E_\theta(r,\theta) = \sum_n \frac{1}{r}\left[D_n F'_{\nu_n}(\cos(\theta) + E_n R'_{\nu_n}(\cos(\theta)) + \frac{V_e^+ + V_e^-}{\sin(\theta)}\frac{e_n}{-\mathrm{i}\omega\varepsilon_0}\right]$$
$$\times \frac{-n\pi}{R_\mathrm{M}-R_\mathrm{m}}\sin\left(\frac{(r-R_\mathrm{m})n\pi}{R_\mathrm{M}-R_\mathrm{m}}\right), \tag{A.12}$$
$$H_\varphi(r,\theta) = -j\omega\varepsilon_0 \sum_n \left[D_n F'_{\nu_n}(\cos(\theta) + E_n R'_{\nu_n}(\cos(\theta)) + \frac{V_e^+ + V_e^-}{\sin(\theta)}\frac{e_n}{-\mathrm{i}\omega\varepsilon_0}\right]$$
$$\times \frac{1}{r}\cos\left(\frac{(r-R_\mathrm{m})n\pi}{R_\mathrm{M}-R_\mathrm{m}}\right).$$

In the coaxial–SGW junction on the drain side, the same development can be made with the results:

$$E_r(r,\theta) = \sum_n \left[G_n F_{\nu_n}(\cos(\pi-\theta) + I_n R_{\nu_n}(\cos(\pi-\theta))\right]$$
$$\times \left(\left(\frac{n\pi}{R_\mathrm{M}-R_\mathrm{m}}\right)^2 + k_0^2\right)\left(-\cos\left(\frac{(r-R_\mathrm{m})n\pi}{R_\mathrm{M}-R_\mathrm{m}}\right)\right),$$
$$E_\theta(r,\theta) = \sum_n \frac{1}{r}\left[G_n F'_{\nu_n}(\cos(\pi-\theta) + I_n R'_{\nu_n}(\cos(\pi-\theta)) + \frac{V_s^+ + V_s^-}{\sin(\theta)}\frac{e_n}{-\mathrm{i}\omega\varepsilon_0}\right]$$
$$\times \frac{-n\pi}{R_M - R_m}\sin\left(\frac{(r-R_\mathrm{m})n\pi}{R_\mathrm{M}-R_\mathrm{m}}\right), \tag{A.13}$$
$$H_\varphi(r,\theta) = -j\omega\varepsilon_0 \sum_n \left[G_n F'_{\nu_n}(\cos(\pi-\theta) + I_n R'_{\nu_n}(\cos(\pi-\theta)) + \frac{V_s^+ + V_s^-}{\sin(\theta)}\frac{e_n}{-\mathrm{i}\omega\varepsilon_0}\right]$$
$$\times \frac{1}{r}\cos\left(\frac{(r-R_\mathrm{m})n\pi}{R_\mathrm{M}-R_\mathrm{m}}\right).$$

A.5. Transmitted and non-transmitted modes

Different modes inside the sphere (region 2 of figure A.1) are defined by $\nu_n = \alpha_n + \mathrm{i}\beta_n$ (see (A.4)), which is, in general, a complex number. In accordance with the asymptotic expression

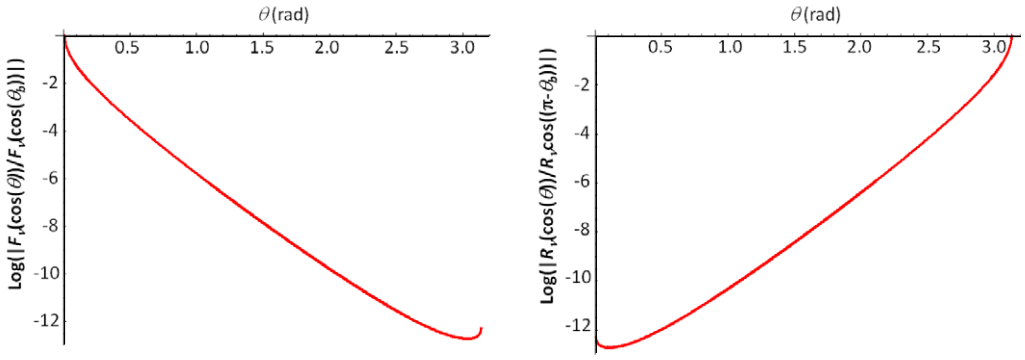

Figure A.2. Graphs for $\mathrm{Log}(|F_{\nu_n}(\cos(\theta))/F_{\nu_n}(\cos(\theta_b))|)$ and $\mathrm{Log}(|R_{\nu_n}(\cos(\theta))/R_{\nu_n}(\cos(\pi-\theta_b)|)$ as a function of θ for $\nu_n = -0.5+4.0j$. $F_{\nu_n}(\cos(\theta))$ and $R_{\nu_n}(\cos(\theta))$ have a near-exponential attenuation similar to the evanescent waves in conventional waveguides. The modes with complex ν_n are not transmitted. The only modes that exist inside the SWG far from the interface are the modes having real ν_n. For the band of frequencies and dimensions analyzed here, only ν_0 is real and the guide works as single-mode.

of Legendre functions $P_{\nu_n}(x)$ and $Q_{\nu_n}(x)$ for x close to 1 and -1, the following results are obtained [30]:

$$\left|\frac{F_{\nu_n}(\cos(\pi-\theta))}{F_{\nu_n}(\cos(\theta))}\right| \to \mathrm{e}^{-\beta_n}, \qquad \left|\frac{R_{\nu_n}(\cos(\theta))}{R_{\nu_n}(\cos(\pi-\theta))}\right| \to \mathrm{e}^{-\beta_n}, \quad \text{for} \quad \theta \to 0,$$

$$\beta_n = \mathrm{Im}[\nu_n]. \tag{A.14}$$

Bearing in mind the SGW dimension and the frequencies of interest (the microwave frequencies from 0.2 to 0.4 GHz), the parameter ν_n is real only for $n = 0$. For example, for $f = 300$ MHz, $\nu_0 = 4.98$, $\nu_1 = -0.5+631.4\mathrm{i}$, $\nu_2 = -0.5+1262.9\mathrm{i}$ and so on. Figure A.2 shows the graphs for $\mathrm{Log}(|F_{\nu_n}(\cos(\theta))/F_{\nu_n}(\cos(\theta_b))|)$ and $\mathrm{Log}(|R_{\nu_n}(\cos(\theta))/R_{\nu_n}(\cos(\pi-\theta_b))/|)$ with respect to θ for a complex value $\nu_n = -0.5+4.0\mathrm{i}$ (θ_b is defined in figure A.1). Clearly $|F_{\nu_n}(\cos(\theta))|$ suffers a near-exponential attenuation between $\theta = \theta_b$ and $\theta = \pi - \theta_b$ as shown in (A.14). The same thing occurs for $|R_{\nu_n}(\cos(\theta))|$ between $\theta = \pi - \theta_b$ and $\theta = \theta_b$. Similar results are found for every complex permittivity ν_n, so $F_{\nu_n}(\cos(\theta))$ and $R_{\nu_n}(\cos(\theta))$ can be considered as evanescent waves. The SWG works as a single mode with the fields and transmitted power far from the interface region given by the equations (2) and (3).

A.6. Boundary conditions

The coefficients A_n and B_n from (A.4), D_n and E_n from (A.6) and G_n and I_n from (A.13) are obtained using the following boundary conditions (figure A.1):

- The tangent electric field in the inner conductor surface is null.
- The electric and magnetic fields are the same in the common surface between regions 2 and 3.
- The same conditions in the coaxial on the drain side.

$$
\begin{aligned}
&D_n F_{\nu_n}(\cos(\theta_a)) + E_n R_{\nu_n}(\cos(\theta_a)) = 0,\\
&D_n F_{\nu_n}(\cos(\theta_b)) + E_n R_{\nu_n}(\cos(\theta_b)) = A_n F_{\nu_n}(\cos(\theta_b)) + B_n R_{\nu_n}(\cos(\theta_b)),\\
&D_n F'_{\nu_n}(\cos(\theta_b)) + E_n R'_{\nu_n}(\cos(\theta_b)) + \frac{V_e^+ + V_e^-}{\sin(\theta_b)} \frac{e_n}{-\mathrm{i}\omega\varepsilon_0} = A_n F'(\cos(\theta_b)) + B_n R'_{\nu_n}(\cos(\theta_b)),\\
&G_n F_{\nu_n}(\cos(\pi-\theta_a)) + I_n R_{\nu_n}(\cos(\pi-\theta_a)) = 0\\
&G_n F_{\nu_n}(\cos(\pi-\theta_b)) + I_n R_{\nu_n}(\cos(\pi-\theta_b)) = A_n F_{\nu_n}(\cos(\pi-\theta_b)) + B_n R_{\nu_n}(\cos(\pi-\theta_b)),\\
&G_n F'_{\nu_n}(\cos(\pi-\theta_b)) + I_n R'_{\nu_n}(\cos(\pi-\theta_b)) + \frac{V_s^+ + V_s^-}{\sin(\pi-\theta_b)} \frac{e_n}{-\mathrm{i}\omega\varepsilon_0} = A_n F'_{\nu_n}(\cos(\pi-\theta_b)\\
&\qquad + B_n R'_{\nu_n}(\cos(\pi-\theta_b)),
\end{aligned}
\tag{A.15}
$$

where θ_a and θ_b are as defined in figure A.1. When the voltages in the two coaxial lines ($V_e = V_e^+ + V_e^-$ and $V_s = V_s^+ + V_s^-$) are known, the system (A.15) can be solved for each n.

A.7. Perfect drain

In accordance with the previous analysis, the SGW works as a single-mode guide, so the condition for the perfect drain (no reflected wave in the guide) is satisfied when $B_0 = 0$ in (A.4). The procedure to obtain the perfect drain consists of the following steps:

- In (A.15) for $n = 0$, the condition $B_0 = 0$ is imposed. Then A_0, D_0, E_0, G_0, I_0 and $V_s^+ + V_s^-$ are calculated. $V_s^+ + V_s^-$ is the necessary voltage (on the coaxial drain side) for perfect wave absorption in the load.
- The coefficients A_n, B_n, D_n, E_n, G_n and I_n are obtained using (A.15) and the voltage $V_s^+ + V_s^-$ calculated in the previous step.
- The field H_φ for $r = R_\mathrm{M}$ and $\theta_a < \theta < \theta_b$ is computed using (A.12).
- For the sake of uniqueness of the solution, this field has to depend on θ as in (A.3). The voltage $V_s^+ - V_s^-$ is then obtained.
- The impedance of the coaxial line at $r = R_\mathrm{M}$ and the load are

$$
Z_S = Z_0 \frac{V_s^+ + V_s^-}{V_s^+ - V_s^-}, \qquad Z_\mathrm{pd} = Z_0 \frac{V_s^+ \mathrm{e}^{\mathrm{i}k_0 L} + V_s^- \mathrm{e}^{-\mathrm{i}k_0 L}}{V_s^+ \mathrm{e}^{\mathrm{i}k_0 L} - V_s^- \mathrm{e}^{-\mathrm{i}k_0 L}}. \tag{A.16}
$$

The results of the calculation of the real and imaginary parts of the perfect drain impedance for the band of frequencies of interest are shown in figure 3. Figure A.3 shows a comparison between the modulus of the theoretical electric field (in the case of the perfect drain, only the forward wave exists there, given by the function $F_{\nu_n}(\theta)$) and the modulus of the electric field simulated in COMSOL. Figure A.3 shows excellent matching between the theoretical and simulated fields for $f = 0.25$ GHz. For this simulation, the circuit parameters have been calculated using the linear approximations presented in figure 3 ($R = 2.57\Omega$ and $C = 55.05$ pF). Table A.1 shows the values of the constant ν_n (see (A.4)) and the electric field E_n for the first reflected modes in $\theta = \pi - \theta_b$, that is, the value

$$
E_n = B_n R_{\nu_n}(\cos(\pi - \theta_b)) \left(\left(\frac{n\pi}{R_\mathrm{M} - R_\mathrm{m}} \right)^2 + k_0^2 \right) \ (V/m). \tag{A.17}
$$

Table A.1. The reflected electric field E_n and the constant ν_n for the first ten modes in $\theta = \pi - \theta_b$. When $n = 0$, E_n is zero because the load has been designed with the condition $B_0 = 0$. These modes given by $n = 1, 2, \ldots, 9$ are evanescent, so they have quasi-exponential decay from receptor $\theta = \pi - \theta_b$ toward emitter $\theta = \theta_b$. The electric field is approximately attenuated as $e^{-\beta_n \frac{\theta}{2\pi}}$; see equation (A.14) and figure A.2.

n	$\nu_n = \alpha_n + i\beta_n$	E_n	n	$\nu_n = \alpha_n + i\beta_n$	E_n
0	4.7598	0.0 + 0.0i	1	−0.5 + 631i	4.161 65 − 0.628 369i
2	−0.5 + 1263i	−3.491 57 + 0.525 264i	3	−0.5 + 1894i	−1.769 05 + 0.251 193i
4	−0.5 + 2526i	−1.756 42 + 0.259 907i	5	−0.5 + 3157i	0.659 417 − 0.096 345i
6	−0.5 + 3789i	−0.346 259 + 0.050 4032i	7	−0.5 + 4420i	0.470 42 − 0.068 5852i
8	−0.5 + 5052i	0.380 658 − 0.054 9126i	9	−0.5 + 5683i	0.380 658 − 0.054 9126i

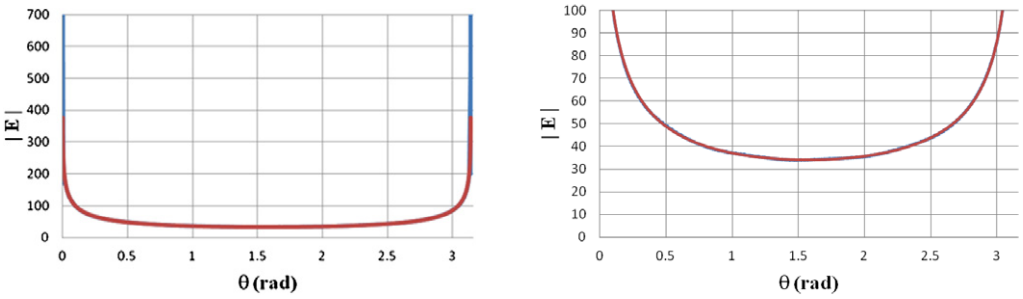

Figure A.3. Left: the modulus of the theoretic electric field (in red) and the modulus of the electric field simulated in COMSOL (in blue) for the SGW with the perfect drain. Right: close-up of the same graphs.

Appendix B. Voltage and current waves inside the spherical geodesic waveguide

When the drain port is centered at the source's image point, from the fields of the incident and reflected modes we can define the incident and reflected voltage and current waves, similarly to classical microwave transmission lines. They are defined as follows:

$$
\begin{aligned}
V_{\mathrm{i}}(\theta) &= \int_{R_{\mathrm{m}}}^{R_{\mathrm{M}}} k_0^2 A F_\nu(\cos(\theta))\,\mathrm{d}r = k_0^2 A (R_{\mathrm{M}} - R_{\mathrm{m}}) F_\nu(\cos(\theta)),\\
V_{\mathrm{r}}(\theta) &= \int_{R_{\mathrm{m}}}^{R_{\mathrm{M}}} k_0^2 A R_\nu(\cos(\theta))\,\mathrm{d}r = k_0^2 B (R_{\mathrm{M}} - R_{\mathrm{m}}) R_\nu(\cos(\theta)),\\
I_{\mathrm{i}}(\theta) &= \int_0^{2\pi} \frac{-j\omega\varepsilon_0}{r} A \frac{\mathrm{d}F_\nu(\cos(\theta))}{\mathrm{d}\theta} r\sin(\theta)\,\mathrm{d}\varphi = -j\omega\varepsilon_0 2\pi A \frac{\mathrm{d}F_\nu(\cos(\theta))}{\mathrm{d}\theta}\sin(\theta),\\
I_{\mathrm{r}}(\theta) &= \int_0^{2\pi} \frac{-j\omega\varepsilon_0}{r} A \frac{\mathrm{d}R_\nu(\cos(\theta))}{\mathrm{d}\theta} r\sin(\theta)\,\mathrm{d}\varphi = -j\omega\varepsilon_0 2\pi B \frac{\mathrm{d}R_\nu(\cos(\theta))}{\mathrm{d}\theta}\sin(\theta).
\end{aligned}
\tag{B.1}
$$

Then, the transmitted power expressed in (3) can be obtained from (B.1) as

$$P = \tfrac{1}{2}\mathrm{Re}[V I^*] = \tfrac{1}{2}\mathrm{Re}[(V_\mathrm{i}(\theta) + V_\mathrm{r}(\theta))(I_\mathrm{i}(\theta) + I_\mathrm{r}(\theta))^*]. \tag{B.2}$$

References

[1] Fang N, Lee H, Sun C and Zhang X 2005 Sub-diffraction-limited optical imaging with a silver superlens *Science* **308** 534–7

[2] Mesa F, Freire F, Marqués R and Baena J D 2005 Three dimensional superresolution in material slab lenses: experiment and theory *Phys. Rev.* B **72** 235117

[3] Pendry J B 2000 Negative refraction makes a perfect lens *Phys. Rev. Lett.* **85** 3966–89

[4] Shelby R A, Smith D R and Schultz S 2001 Experimental verification of negative index of refraction *Science* **292** 79

[5] Wiltshire M C, Pendry J B, Young I R, Larkman D J, Gilderdale D J and Hajnal J V 2001 Microstructured magnetic materials for radio frequency operation in magnetic resonance imaging (MRI) *Science* **291** 848

[6] Born M and Wolf E 1997 *Principles of Optics* 6th edn (Cambridge: Cambridge University Press) p 143

[7] Leonhardt U 2009 Perfect imaging without negative refraction *New J. Phys.* **11** 093040

[8] Leonhardt U and Philbin T G 2010 Perfect imaging with positive refraction in three dimensions *Phys. Rev.* A **81** 011804

[9] Benítez P, Miñano J C and González J C 2010 Perfect focusing of scalar wave fields in three dimensions *Opt. Express* **18** 7650–63

[10] Blaikie R J 2010 Comment on 'Perfect imaging without negative refraction' *New J. Phys.* **12** 058001

[11] Leonhardt U 2010 Reply to comment on 'Perfect imaging without negative refraction' *New J. Phys.* **12** 058002

[12] Guenneau S, Diatta A and McPhedran R C 2010 Focusing: coming to the point in metamaterials *J. Mod. Opt.* **57** 511–27

[13] Merlin R 2010 Comment on perfect imaging with positive refraction in three dimensions *Phys. Rev.* A **82** 057801

[14] Sun F and He S 2010 Can Maxwell's fish eye lens really give perfect imaging? *Prog. Electromagn. Res.* **108** 307–22

[15] Sun F, Ge X C and He S 2010 Can Maxwell's fish eye lens really give perfect imaging? II. The case with passive drains *Prog. Electromagn. Res.* **110** 313–28

[16] Leonhardt U and Sahebdivan S 2010 Perfect imaging: they do not do it with mirrors *J. Opt.* **13** 024016

[17] Leonhardt U and Philbin T G 2010 Reply to comment on 'Perfect imaging with positive refraction in three dimensions' *Phys. Rev.* A **82** 057802

[18] Kinsler P and Favaro A 2011 Comment on: reply to comment on 'Perfect imaging without negative refraction' *New J. Phys.* **13** 028001

[19] Leonhardt U 2011 Reply to comment on reply to comment on 'Perfect imaging without negative refraction' *New J. Phys.* **13** 028002

[20] González J C, Benítez P and Miñano J C 2011 Perfect drain for the Maxwell fish eye lens *New J. Phys.* **13** 023038

[21] Ma YG, Ong CK, Sahebdivan S, Tyc T and Leonhardt U 2010 Perfect imaging without negative refraction for microwaves arXiv:1007.2530v1

[22] Ma Y G, Sahebdivan S, Ong C K, Tyc T and Leonhardt U 2011 Evidence for subwavelength imaging with positive refraction *New J. Phys.* **13** 033016

[23] Miñano J C, Marqués R, González J C, Benítez P, Delgado V, Grabovickic D and Freire M 2011 Super-resolution for a point source better than $\lambda/500$ using positive refraction *New J. Phys.* **13** 125009

[24] Miñano J C, Benítez P and González J C 2010 Perfect imaging with geodesic waveguides *New J. Phys.* **12** 123023

[25] Leonhardt U 2010 *Geometry and Light: The Science of Invisibility* (New York: Dover)
[26] Pozar D M 2005 *Microwave Engineering* (New York: Wiley)
[27] Nussenzveig H M 1965 High-frequency scattering by an impenetrable sphere *Ann. Phys.* **34** 23
[28] Wu D and Ruan C 1998 Analysis on a radial-line/coaxial-line junction *Electron. Lett.* **34** 994
[29] Ishimaru A 1991 *Electromagnetic Wave Propagation, Radiation and Scattering* (Englewood Cliffs, NJ: Prentice-Hall)
[30] Erdélyi A, Magnus W, Oberhettinger F and Tricomi F G 1953 *Higher Transcendental Functions* vol 1 (New York: McGraw-Hill)
[31] Jackson D J 1998 *Classical Electrodynamics* 3rd edn (New York: Wiley)
[32] Solimeno S, Crosignani B and DiPorto P 1986 *Guiding, Diffraction and Confinement of Optical Radiation* (New York: Academic)